RSC Advances

PAPER

View Article Online
View Journal | View Issue

Cite this: *RSC Adv.*, 2022, **12**, 6831

Investigation of optical and electrical properties of the semiconducting α-$KZnPO_4$ compound

N. Chakchouk, Kh. Ben Brahim, M. Ben Gzaiel and A. Oueslati

Received 20th January 2022
Accepted 23rd February 2022

DOI: 10.1039/d2ra00426g

rsc.li/rsc-advances

We used the solid state method to synthesize the α-$KZnPO_4$ compound. The X-ray diffraction pattern revealed that the sample represents a single hexagonal phase with a $P6_3$ space group. The chemical composition of the compound was examined by energy dispersive spectroscopy. The optical absorption measurement confirmed the semiconductor nature of the compound with a band gap around 4.52 eV. Furthermore, the electrical properties of the material were analyzed by means of the impedance spectroscopy, in a frequency range from 100 Hz to 1 MHz and a temperature range from 583 K to 673 K. The dependency of $s(T)$ on temperature showed that the overlapping large polaron tunneling model is the mechanism responsible for AC conduction in the compound. A correlation between the crystal structure and the ionic conductivity was established and discussed. Finally, the temperature variation of M'' peak showed a thermally activated relaxation process and a temperature-dependent stretching exponent β parameter.

1. Introduction

In the last few years, numerous research studies have emphasized phosphate-based materials, not only by understanding their characteristics but also by studying their different technological applications.[1–3] A particular interest has been devoted to the orthophosphate materials with formula $ABPO_4$ (A = Na, Li, Ag, K… and B = Zn, Fe, Ni, Co,…) thanks to their interesting properties, as well as their excellent thermal stability, hydrolytic stability and charge stabilization.[4,5] Among them, we can mention the optical and ferroelectric properties.[6,7] Moreover, researchers have put the light on the specific characteristic of the orthophosphate that comprehended a monovalent cation thanks to their significant ionic conductivity and potential value as solid electrolytes for rechargeable "alkaline batteries".[8–10] In addition the crystal structure diversity is a principal feature for this family of compounds that are controlled by the stereochemical behaviors of the A and B cations. Among the different structures, we are interested in the tridymite type materials that possess a strong correlation between structural, physical and electrochemical properties.[11]

In this research paper, we are interested in the study of the $KZnPO_4$. This compound undergoes two phase transitions at 691 °C and 783 °C where two allotropic forms can be distinguished which are the β-$KZnPO_4$ (medium-temperature) and γ-$KZnPO_4$ (high-temperature).[12] The α-$KZnPO_4$ compound has previously been reported to crystallize the hexagonal space group $P6_3$.[12,13] The β-$KZnPO_4$ structure is in the orthorhombic system with space group $Pna2_1$. As for the γ-$KZnPO_4$ structure, it maintains the orthorhombic system only changing its space group to *Pnma*. The different structures of the compound display the properties of the stuffed tridymite family and have a tetrahedral skeleton. The α–β transition occurs by tetrahedral reversal while the β–γ transition is a displace phenomenon with a ferroelectric character. The topology of the α-$KZnPO_4$ compound is in the UUUDDD-ring form (point up "*U*", point down "*D*") where these rings are formed by the PO_4 and ZnO_4 tetrahedra in an alternative way. These rings are occupied by the K^+ cations.[14–16]

To our knowledge, no conductivity and vibrational behavior studies have been carried out for the studied compound. As a continuation to the previous structural study that have been reported and to further understand the physical properties of this compound, we have studied the structural, morphological and electrical properties. A correlation between the crystal structure and ionic conductivity has been established and discussed. In addition, the optical measurements by UV-vis absorption were performed.

2. Experimental methods

2.1 Synthesis procedure

The polycrystalline sample of α-$KZnPO_4$ was prepared *via* the conventional solid-state reaction method by mixing high purity precursors of K_2CO_3 (99.9% purity), ZnO (99.9% purity) and $(NH_4)_2HPO_4$ (99.9% purity) in the desired proportion according to the following reaction:

U, niversity of Sfax, Laboratory of Spectroscopic Characterization and Optics of Materials, Faculty of Sciences, B. P. 1171, 3000, Sfax, Tunisia. E-mail: narimenchakchouk@yahoo.fr

$$K_2CO_3 + 2ZnO + 2(NH_4)_2HPO_4 \rightarrow 2KZnPO_4 + CO_2 + 4NH_3 + 3H_2O \quad (1)$$

In this context, the starting reagents were mixed and intimately ground in an agate mortar for 30 min to ensure the best homogeneity and reactivity. After that, the homogenized powder, was firstly calcined in an electric furnace at a temperature of 573 K for 8 h, in order to exhaust CO_2, NH_3, and H_2O. Further, the calcined powder was grounded again for 8 h, and then pressed into cylindrical pellets, having a diameter of 7.78 mm, using a 2.94×10^8 Pa uniaxial pressure to promote the reaction. Finally, the white pellets were sintered at 873 K for 20 h and then cooled slowly at a rate of 5 K min^{-1} at room temperature. It is noticed all stages occurring sequentially as the sintering temperature increases: a formation of isthmuses between grains, a compaction of grains, and finally, their growth.

2.2 Characterization techniques

The crystal phase and purity of the α-$KZnPO_4$ compound were characterized by X-ray powder diffraction (XRD) using a Panalytical X'Pert Prompd diffractometer equipped with copper radiation CuK_α ($\lambda = 1.54060$ Å) recorded at room temperature. The intensity data were recorded by continuous scan in $2\theta/\theta$ mode from 10° to 85° with a step $\Delta(2\theta) = 0.017°$. XRD was analyzed by the Rietveld method using the "FullProf" software.

The chemical analysis of the sample shaped into pellets was carried out by EVO LS10 (Zeiss) scanning electron microscopy connected with the energy dispersive system: INCA (Oxford Instruments).

The optical spectrum of the investigated compound was carried out at room temperature using a UV-3101PC scanning spectrophotometer (Integrated Sphere) in the wavelength range 200–800 nm with a resolution of 0.5 nm.

Furthermore, the electrical measurements were performed on a sintered pellet having a typical dimension of 7.78 mm in diameter and 1.20 mm in thickness. The opposite sides of this pellet were coated with a conducting silver paint to ensure a high electrical contact. The transport properties of the sample were examined by AC impedance spectroscopy using an 1260 Solartron Impedance Analyzer under vacuum operating over a frequency range of 100 Hz to 1 MHz and at a temperature range of 583 K to 673 K with an AC voltage of 1 V.

3. Results and discussions

3.1 XRD analysis

To analyze the purity of the synthesized compound and obtain the crystalline parameters, an XRPD pattern collected at room temperature was carried out. The refinement of the pattern was performed by the Le Bail method using the fullProf program. The cell parameters and the $P6_3$ space group reported in the bibliographic date were used as a starting point.[13]

Fig. 1 exposes the observed and calculated diffractograms for α-$KZnPO_4$ as well as the corresponding discrepancies. All Bragg peaks were successfully indexed and satisfactorily modeled,

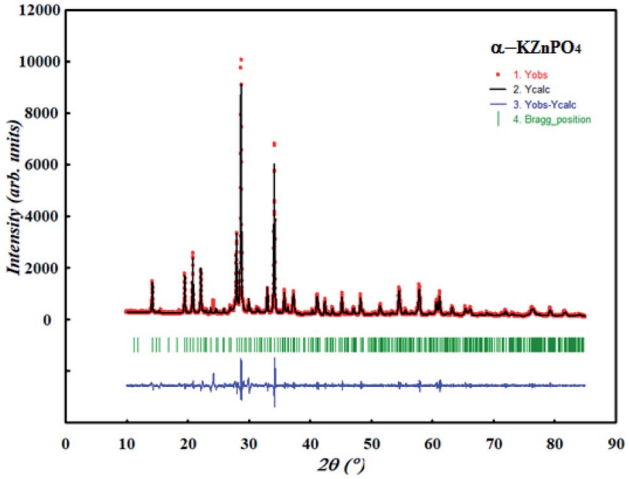

Fig. 1 X-ray diffraction (XRD) of α-$KZnPO_4$ at room temperature: experimental data in red, calculated data in black, difference between them in blue line is shown at the lowest of the diagram and the Bragg positions in green are marked by vertical bar.

thus proving the high purity of the sample. The quality factor which shows the good agreement between the experimental (red points) and calculated (black solid line) profiles is $\chi^2 = 3.24$. The profile parameters are $a = 18.157(2)$ Å, $b = 18.157(2)$ Å, $c = 8.508(2)$ Å and $V = 2429.552(4)$ $Å^3$; $Z = 24$, are in good agreement with the results reported by Andratschke and *et al.*[13] The absence of secondary phase and peaks of impurities confirms that we have produced a pure and good quality compound.

The average crystallite size D of the α-$KZnPO_4$ was calculated by the X-ray peak broadening method using the Williamson–Hall technique (W–H) according to the following equation:[17]

$$\beta_{2\theta} \cos\theta = \frac{K\lambda}{D} + 4\varepsilon \sin\theta \quad (2)$$

where $\beta_{2\theta}$ is the full width at half maximum (FWHM) of the peaks, θ means the Bragg angle, K is the Debye–Scherrer constant (0.9), λ designate the X-ray wavelength, and ε is the average microstrain.

A linear plot of $\beta \cos\theta$ against $4 \sin\theta$ is displayed in Fig. 2. The slope of the linearly adjusted data yields the strain was found 9.69×10^{-4} and the value of interception denotes the crystallite size which is predestined 81 nm.

The dislocation density (δ) gives an idea about the number of defects in the studied sample. It is calculated by using the equation:[18]

$$\delta = \frac{1}{D^2} \quad (3)$$

The dislocation density values is 1.52×10^{-4} nm^{-2}.

3.2 EDX analysis

The chemical compositions of α-$KZnPO_4$ compound were verified by using the energy dispersive spectroscopy. The spectrum shown in Fig. 3 confirms the presence of all the constituent

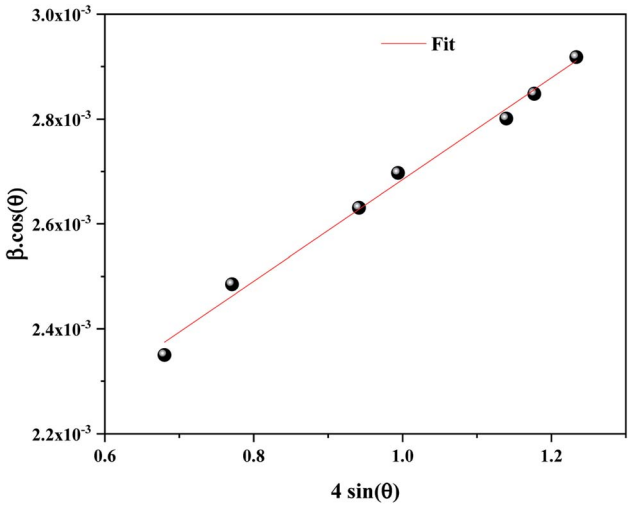

Fig. 2 Williamson–Hall plot of the α-$KZnPO_4$ compound.

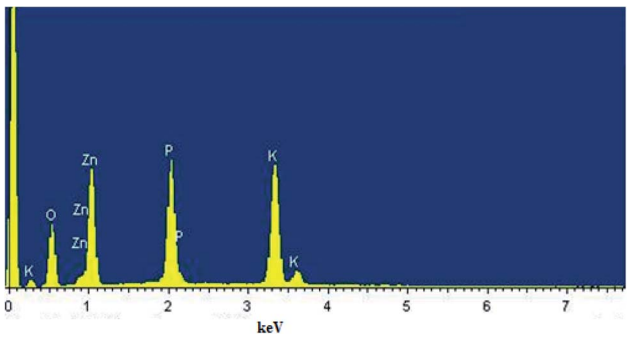

Fig. 3 EDS profile of the ceramic compound α-$KZnPO_4$.

elements of α-$KZnPO_4$, namely, Oxygen (O), Phosphate (P), Zinc (Zn), and Potassium (K), indicating that there was no loss of elements during the sintering step. The proportions of the constituents obtained as atomic percentages are registered in Table 1. The EDX data indicate that the preparation has good stoichiometries property and a purity chemical composition. The EDX and XRPD results confirm the success of synthesis of α-$KZnPO_4$ specimen without any impurity.

3.3 UV/vis spectroscopy

To explore the semiconducting properties of α-$KZnPO_4$, a solid-state UV-vis spectroscopy analysis was performed. Fig. 4 reveals the experimental UV-vis absorption spectrum collected in the 200–800 nm wavelength range, at room temperature. Three

Table 1 Mass and atomic percentages of chemical elements

Chemical element	%Weight	%Atomic
O	33.97	58.95
K	18.49	13.13
P	16.38	14.69
Zn	31.16	13.24

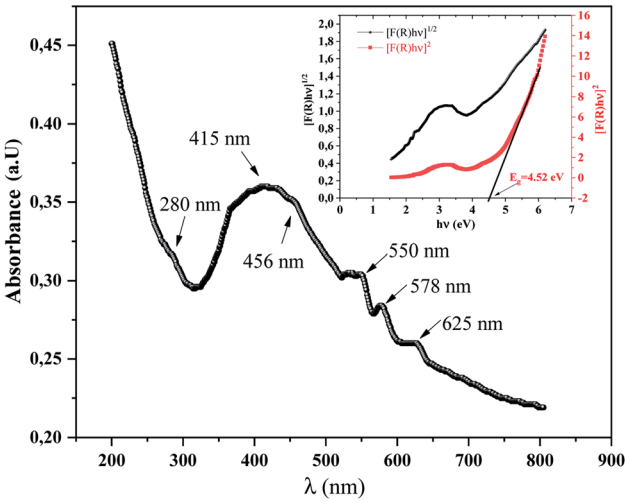

Fig. 4 UV-vis absorption of α-$KZnPO_4$ compound. Insert: the Tauc plot.

bands appearing at 415, 456 nm and at 578 nm correspond to the transitions of the tetrahedron $[PO_4]^{3-}$. These bands can be relative to the electronic transitions $^1T_1 \rightarrow {}^1A_1$, $^3T_2 \rightarrow {}^1A_1$ and $^3T_1 \rightarrow {}^1A_1$, respectively.[19] They are accompanied by the transfer of charges from the oxygen atoms to the central phosphate atom within the $[PO_4]^{3-}$ groups (orbit (2p) of the oxygen ion to the orbit ($3d^0$) of the phosphate ion). Another band observed at 280 nm corresponds to the electronic transitions of the valence band represented by the orbit ($3d^{10}$) of the zinc ion to the conduction band represented by the orbit ($3d^0$) of the phosphate ion, assigned by $^1A_{1g} \rightarrow {}^3T_{1u}$. Thus, two bands at 550 nm and at 625 nm correspond to the zinc ion transitions.[20] The band gap energy of α-$KZnPO_4$ is determined by combining both the Kubelka–Munk function and the Tauc equation, by the following relation:[21,22]

$$F(R)h\nu = \frac{A}{S}(h\nu - E_g)^n \quad (4)$$

where $F(R)$ is equal to $(1 - R)^2/2R$ whither R represents the reflectance, h is Planck's constant, ν is the light frequency, A is a constant according to the probability of transition, n is the index defining the type of transition ($n = 2$ for a permitted indirect transition, $n = 1/2$ for a permitted direct transition, $n = 1/3$ for direct forbidden transition and $n = 3$ for indirect forbidden transition).

The inset of Fig. 4 shows the plots of $(F(R)h\nu)^{1/2}$ and $(F(R)h\nu)^2$ *versus* the photon energy ($h\nu$). The shapes of these curves favor the direct transition. An optical band gap E_g can be determined from the extrapolation of the linear region of the curve to meet the ($h\nu$) axis at $(F(R)h\nu)^2 = 0$. The estimated band gap energy is 4.52 eV. This value proves that the α-$KZnPO_4$ compound is a wide gap semiconductor.

3.4 Electrical properties

3.4.1 Complex impedance spectroscopy. The complex impedance spectroscopy discerns the processes and the

electrical characteristics of compounds. It displays a direct connection between the ideal circuit made by the electrical components and the response of the real system.

Fig. 5 describes the Nyquist diagram ($-Z''$ *vs.* Z') at some temperature. From the shape of these spectra, it can be understood the presence of a single semi-circular arc at each temperature, which confirms the grain contribution in this material.[23] Moreover, the shows that the radius of the corresponding semicircular arcs decreased inversely with temperature, which reveals that the a conductivity improvement and thus more dielectric loss.[24] The material has thus a semiconductor behavior. Additionally, we note that the experimental points are located on the arcs of the circles centered below the real axis. This suggests that the process of conduction in α-$KZnPO_4$ does not obey the Debye model rather the Cole–Cole model.[25]

In order to analyze these spectra and to extract the different electrical parameters, it is useful to have an equivalent circuit model that provides a realistic representation of the electrical properties of the studied sample. The impedance components were adjusted with the Zview software. The best fit is the outcome of an electrical circuit formed by a parallel combination of a resistance R, capacitance C, and fractal capacitance CPE as depicted in the inset of Fig. 5. It is worth mentioning here that the presence of a constant phase element (CPE) in the equivalent circuit model justifies the non-ideal Debye behavior[26] and describes the observed depression of the semicircles.

The impedance of the CPE contribution is an empirical function of the type:

$$Z_{\mathrm{CPE}} = \frac{1}{Q \times (j\omega)^{\alpha}} \tag{5}$$

where ω is the angular frequency, α is a parameter indicating the change of the compressed semicircle from an ideal semicircle and Q is the capacitance value of the CPE element. It is evident that the capacitance values Q are in the range of pF and thus that the single semicircular response is from grain interiors,[27] which is expected from the sample where no grain boundaries are involved. It shows that the electrical phenomena in the sample are the result of the contributions of the grains.[28] The theoretical values of the real (Z') and imaginary ($-Z''$) parts of the complex impedance, derived from the equivalent circuit, were deduced using the following expressions:

$$Z' = \frac{R^{-1} + Q\omega^{\alpha}\cos\left(\frac{\alpha\pi}{2}\right)}{\left(R^{-1} + Q\omega^{\alpha}\cos\left(\frac{\alpha\pi}{2}\right)\right)^2 + \left(C\omega + Q\omega^{\alpha}\ \sin\left(\frac{\alpha\pi}{2}\right)\right)^2} \tag{6}$$

$$-Z'' = \frac{C\omega + Q\omega^{\alpha}\sin\left(\frac{\alpha\pi}{2}\right)}{\left(R^{-1} + Q\omega^{\alpha}\cos\left(\frac{\alpha\pi}{2}\right)\right)^2 + \left(C\omega + Q\omega^{\alpha}\sin\left(\frac{\alpha\pi}{2}\right)\right)^2} \tag{7}$$

The parameters R, α, C, and Q have been obtained by using a mean square method that is used to minimize the difference between the experimental and calculated data.

The justification of the choice of the equivalent circuit is confirmed by the variations of the experimental values of (Z') and ($-Z''$) at various temperatures *versus* the calculated ones

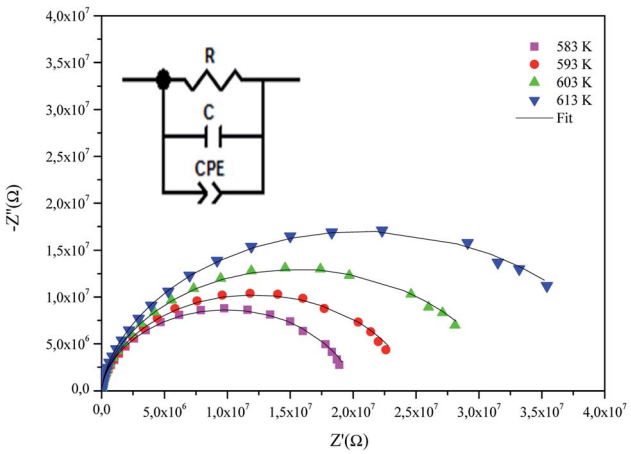

Fig. 5 Complex impedance spectra in the Nyquist plane with electrical equivalent circuit (inset), accompanied by theoretical data (solid line).

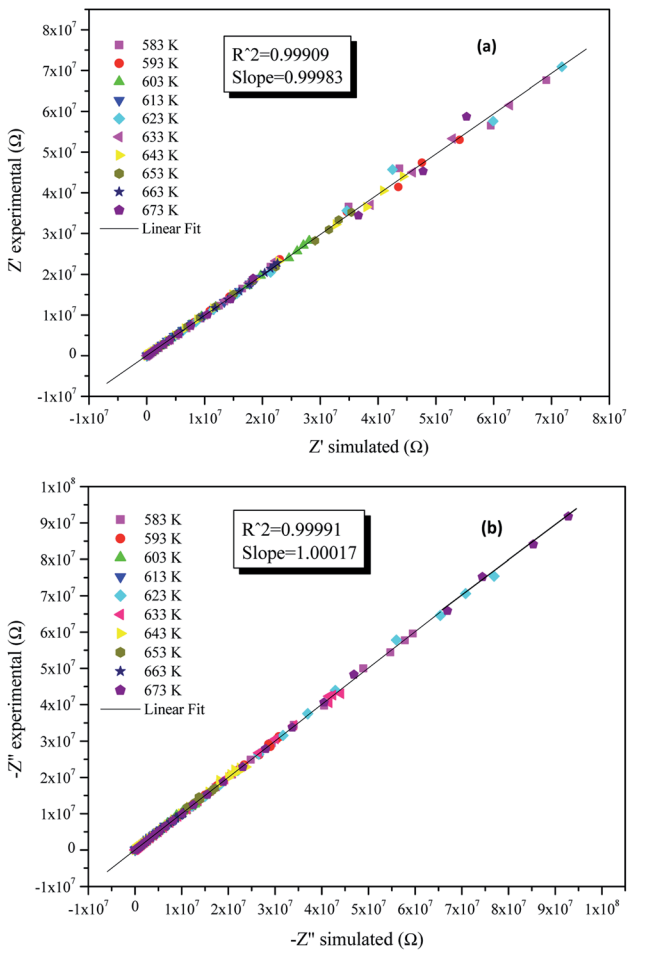

Fig. 6 (a) and (b): plots of measured values *versus* simulated values of the real and imaginary parts of the impedance.

using the parameters of the equivalent circuit model (Fig. 6a and b). From this figure, it is evident that the slope obtained from a linear fit of the data points at each temperature is nearly equal to the unity. This behavior reveals that the adopted equivalent circuit describes well the electric properties of the investigated compound.

3.5 Conductivity studies

3.5.1 DC conductivity. Relying on the bulk resistance values and the sample dimensions, the grain electrical conductivity (σ_{dc}), can be calculated at each temperature using the following equation:[29]

$$\sigma_{dc} = \frac{e}{RS} \quad (8)$$

where e is the thickness of the pellet, S is the area of the electrode deposited on the pellet and R is the value of the bulk resistance determined by the adjustment.

The temperature dependence of the conductivity (σ_{dc}) is displayed in Fig. 7. The linearity of $\ln(\sigma_{dc}T)$ *versus* $1000/T$ justifies that our sample does not have a phase transition in the temperature range studied. We note that the value of the conductivity increases gradually with increasing temperature, suggesting that the electrical conduction in this material is a thermally activated transport process.[30] The linear region is fitted with the Arrhenius equation:

$$\sigma_{dc}T = A \exp\left(-\frac{E_a}{k_B T}\right) \quad (9)$$

where E_a represents the activation energy of conductivity, A is the pre-exponential factor which includes the charge carrier mobility and density of states, k_B is the Boltzmann constant and T is the absolute temperature. The value of activation energy evaluated from the Arrhenius plot for σ_{dc} is about $E_a = (0.91 \pm 0.02)$ eV.

3.5.2 AC electrical conductivity. The AC electrical conductivity is calculated using the real (Z') and the imaginary ($-Z''$) parts of the complex impedance (Z^*) data at a fixed temperature, according to the following expression:

$$\sigma_{ac}(\omega) = \frac{e}{S} \times \frac{Z'}{Z'^2 + Z''^2} \quad (10)$$

The variation of the ac conductivity as a function of the angular frequency at the temperature range from 583 to 673 K is illustrated in Fig. 8. In fact, the conductivity curves reveal the low-frequency and high-frequency regions.

The conductivity σ_{ac} increases gradually with the increase in frequency in the high frequency region. However, it is nearly independent in the low frequency region. We deduce that the ions influence uncorrelated and aleatory hopping motions and lead a macroscopic transport of dc conductivity.[31]

The curves also reveal a AC conductivity elevation in congruence with temperature, which points out the semiconductor behavior of the title compound.[32] In fact, this increase is related to the intensification of the mobility and the charge carriers that favor better conduction.[33]

Added to this, we noticed that the experimental measurements of the AC conductivity can be fitted by the known augmented Jonscher's relation:[34]

$$\sigma_{ac}(\omega) = \sigma_{dc} + A\omega^s + B\omega \quad (11)$$

where σ_{dc} is the continuous conductivity at low frequency, A is a coefficient dependent of temperature, B is weakly temperature-dependent term, $\omega = 2\pi f$ is the angular frequency, and s is an exponent dependent on frequency and temperature, which represents the degree of interaction between mobile ions with the networks which enclose them. According to Funke,[35] the value of s might have a physical meaning.

If $s < 1$, the electron jump is related to a displacement with a sudden jump. However, if $s > 1$, the charge carriers jump occurs between adjacent sites.

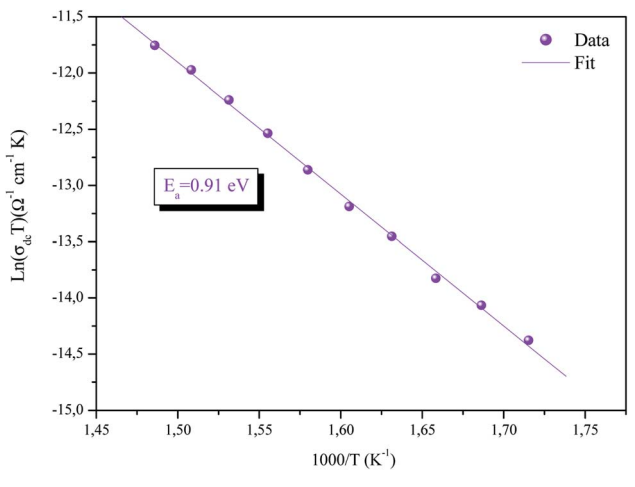

Fig. 7 Arrhenius plots for the bulk conductivity of the α-$KZnPO_4$ sample.

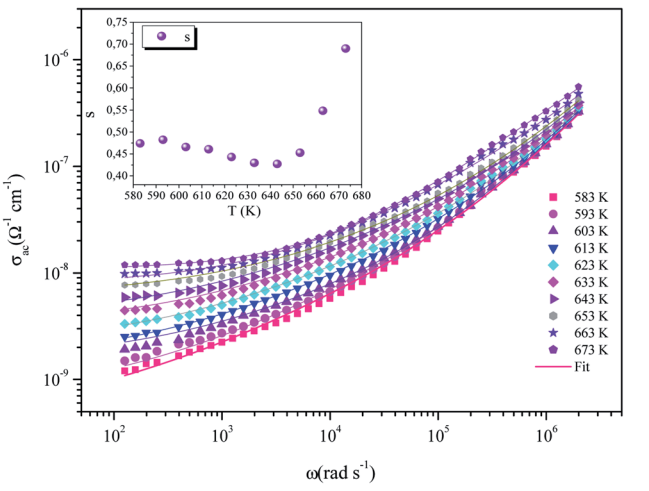

Fig. 8 Dependence of ac conductivity with the angular frequency at different temperatures: the solid lines are the best fits to eqn (9). The inset is the variation of the universal exponent s with the temperature.

Eqn (11) denotes the universal dielectric response (UDR) and the nearly constant loss (NCL), which are two additive terms that match the different processes that occur in the material.

The power-law frequency-dependent UDR term is the result of the hopping of the carriers with interactions of the inherent defects or disorder in the material. However, the linear frequency-dependent NCL term is modeled to originate from rocking motions in an asymmetric double well potential[36] and electrical loss occurring during the time regime; the ions are confined to the potential energy minimum.[37] UDR and NCL terms are also designed to occur in the high-temperature/low-frequency and the low-temperature/high-frequency regimes, respectively.

The modeling of the experimental curves using the Jonscher equation (eqn (11)) shows good agreement between the theoretical and experimental plots and reveals the parameters σ_{dc}, A, B and s at different temperatures.

3.6 AC theory investigation of the conduction mechanism

The dependence of the AC conductivity and its exponent $s(T)$ to frequency and temperature has been explained by a variety of theoretical models. In general, the effect of temperature on the exponent (s) plays a key role in the estimation of the conduction mechanism model in disordered materials. According to the literature, these models are based on tunneling load transport mechanisms by jumping over a potential barrier or through this barrier: these different models are the quantum mechanical tunneling (QMT) model, suggested by Austin-Mott,[38] the correlated barrier hopping (CBH) model, presented by Elliot,[39,40] the overlapping large polaron tunneling (OLPT) model proposed by Long,[41] and finally the small polaron tunneling (SPT) model.[42]

The variation of the exponent s as a function of temperature is shown in the inset of Fig. 8. It shows a drop when the temperature rises, reaching a minimum at 643 K, and then it starts to increase with increasing temperature. According to Long,[41] the overlapping large polaron tunneling model (OLPT) is the adequate model for this compound. In addition, this model can be used in other phosphate compounds such as $NaZnPO_4$ (ref. 43) and α-$AgCuPO_4$.[44]

In this model, the polaron tunneling mechanism endorses the AC conductivity while the distortion clouds of the polarons overlapped. As for large polarons, the spatial extent of the polaron was larger than the interatomic spacing. For some polarons, the potential wells of the nearby sites could overlap due to the long-range character of the Coulomb interaction. Subsequently, the polaron hopping energy decreases. The polaron hopping energy is reduced according to the following equation:

$$W_H = W_{H0}\left(1 - \frac{r_p}{R}\right) \quad (12)$$

where W_H is the polaron hopping energy, the intersite separation R is a random variable, r_p is the radius of the large polaron, and W_{H0} is given by:

$$W_{H0} = \frac{e^2}{4\,\varepsilon_p r_p} \quad (13)$$

According to this model, the expression for the AC conductivity was evaluated by the following equation:[41,43,44]

$$\sigma_{ac}(\omega) = \frac{\pi^4}{12} e^2 (K_B T)^2 N(E_F)^2 \times \frac{\omega (R_\omega)^4}{\left(2\alpha K_B T + \frac{W_{H0} r_p}{(R_\omega)^2}\right)} \quad (14)$$

with $N(E_F)$ is the density of states near the Fermi level and R_ω is the tunneling distance, at a fixed frequency ω it is calculated by resolving the following quadratic equation:

$$R_\omega = \frac{1}{4\alpha}\left\{\ln\left(\frac{1}{\omega\tau_0}\right) - \frac{W_{H0}}{K_B T} + \left[\left(\frac{W_{H0}}{K_B T} - \ln\left(\frac{1}{\omega\tau_0}\right)\right)^2 + \frac{8\alpha W_{H0} r_p}{K_B T}\right]^{\frac{1}{2}}\right\} \quad (15)$$

In the OLPT model, s is defined by the following formula:

$$s = 1 - \frac{8\alpha R_\omega + \frac{6 W_{H0} r_p}{R_\omega K_B T}}{\left(2\alpha R_\omega + \frac{W_{H0} r_p}{R_\omega K_B T}\right)^2} \quad (16)$$

These expressions are used in order to adjust the variation of $\ln(\sigma_{ac})$ as a function of $1000/T$ for fixed values of frequency, which is shown in Fig. 9. It is clear that the theoretical calculations of the conductivity (fits) are in good agreement with the experimental data (symbol), which confirms the choice of the OLPT model.

The values of the parameters α, W_{H0}, $N(E_F)$, r_p, and R_ω, resulting from this adjustment are classified in Table 2.

Among the results of refinement, the variations of the states density $N(E_F)$ against frequency are shown in Fig. 10(a). The frequency increase stimulates the mobility of free charge. This can be the cause behind the increment of the radius of the

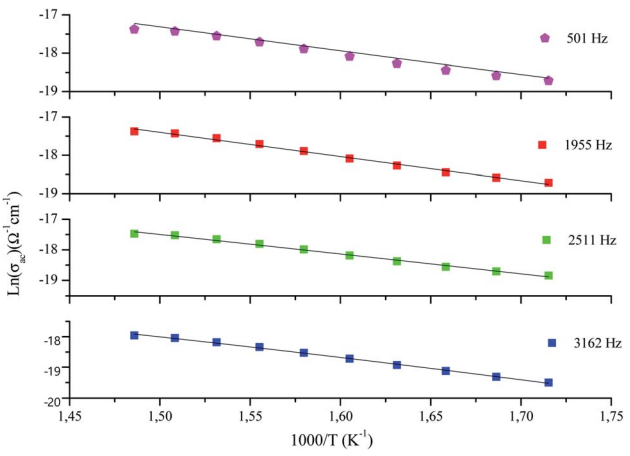

Fig. 9 OLPT model fitting of ac conductivity at different frequency values for α-$KZnPO_4$.

Table 2 Parameters obtained from the fitting of experimental data of total ac conductivity with overlapping large polaron tunneling (OLPT) model for the studied sample

Frequencies (Hz)	$N(E_F)$ (eV^{-1} cm^{-3})	α ($Å^{-1}$)	W_{H0} (eV)	r_p (Å)
501	3.83×10^{13}	1	0.90	0.20
1955	4.00×10^{13}	1	0.97	0.39
2511	4.37×10^{13}	1	0.99	0.46
3162	4.53×10^{13}	1	1.0 3	0.49

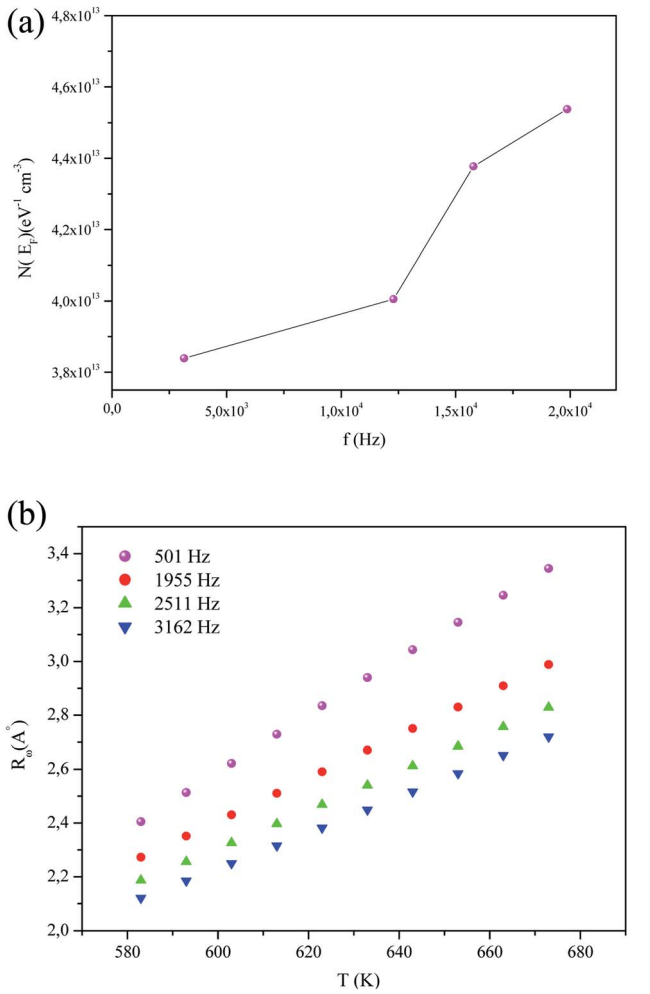

Fig. 10 (a) Variation of the parameters $N(E_F)$ (eV^{-1} cm^{-3}) as a function of frequency. (b) Temperature dependence of the hopping tunneling distance R_ω at different frequencies.

polaron (r_p) and it thus justifying the elevation of the ac conductivity at a high frequency.

The variation of the tuning distance R_ω with temperature for diverse frequencies is illustrated in Fig. 10(b). For a fixed temperature, it is remarkable that the tunneling distance R_ω decreases most rapidly at anincreased frequency. At a fixed frequency, the distance of the tunnel increases with the increase in temperature, implying that the elevation in temperature provides a contribution of thermal energy to the polarons, which then move and accelerate the hopping processes and, subsequently, the interchain interaction.

We notice that the values of R_ω were similar to the interatomic spacing. The R_ω hopping distance are in the interatomic distance (2.10 Å $\leq R_\omega \leq$ 3.34 Å) order of magnitude. The conduction process of the material is due to the movement of the K^+ cation along the (001) tunnels direction.

3.7 Complex modulus analysis

To analyze the electrical relaxation processes at different temperatures and frequencies, we relied on the modulus formalism. This method makes it possible to extract the conductivity relaxation frequency for the grain material and to determine the charge carrier parameters.

This formalism is complementary to the conductivity study.

Macedo and *et al.*[45] formulated a theory for conductivity relaxation in ion conductors in terms of a dimensionless quantity, M^*, which is defined as the inverse of complex permittivity, $\varepsilon^*(\omega)$. It is resolved into real and imaginary parts:

$$M^* = \frac{1}{\varepsilon^*} = j\omega C_0 Z^* = M' + jM'', \quad (17)$$

$$M' = \frac{\varepsilon'}{(\varepsilon'^2 + \varepsilon''^2)}$$

$$M'' = \frac{\varepsilon''}{(\varepsilon'^2 + \varepsilon''^2)}$$

where $C_0 = \frac{S\varepsilon_0}{e}$ is the vacuum capacitance of cell.

The variation of the real part of the electric modulus (M') as afunction of the frequency at different temperatures isshownin Fig. 11(a). At lower frequencies region, M' is found to be approaching zero for all the given temperatures, which may be due to the neglect of electrode polarization.[46] Moreover, the value of M' has followed a continuous dispersal with the increase in frequency. This can be attributed to the conduction phenomena due to the short distance mobility of charge carriers in the temperature ranges considered.[47,48]

The variation of the imaginary part M'' of the modulus as a function of frequency at several temperatures is shown in Fig. 11(b).

The plot shows the characteristic peaks at (f_{max}) centered at the dispersion region of the real part of electric modulus (M'). The presence of these peaks in the modulus spectra accounts for the conductivity relaxation processes. At a higher temperature, the relaxation peak moves to a higher frequency position, which shows a relaxation process in accordance with temperature. With the increase in temperature, the charge carriers become thermally activated and their movement speeds up. Consequently, the relaxation time decreases and the relaxation frequency increases. This phenomenon shifts the relaxation peaks towards a higher frequency with an increasing temperature.

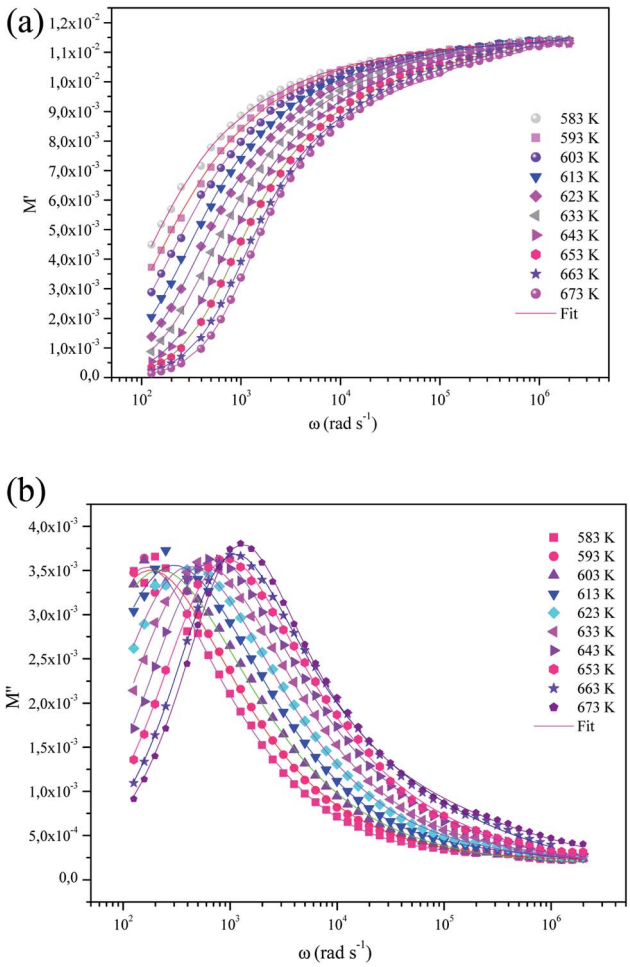

Fig. 11 (a) The variation of the real part of the electrical modulus as a function of the frequencies of α-$KZnPO_4$ at different temperatures. (b) Variation of imaginary parts of modulus (M'') as a function of frequency at various temperatures. Solid lines represent the fitted data to eqn (16).

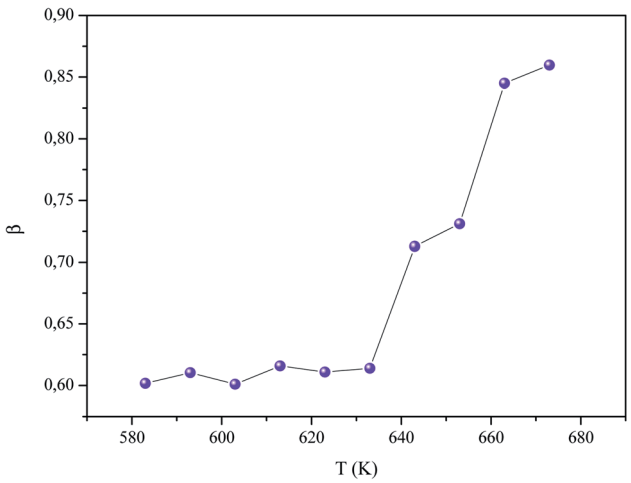

Fig. 12 Variation of β as a function of temperature.

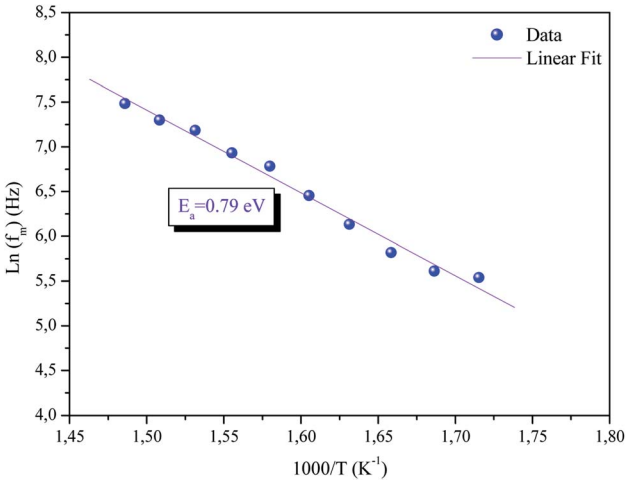

Fig. 13 The dependence of ln(f_m) on temperature for α-$KZnPO_4$.

At the low frequency region below the maximum peak M''_{max}, a pure conduction process takes place.[49] The charge carriers drift to long distances. However, at the high frequency region above the maximum peak M''_{max}; the carriers are spatially constrained to move freely only within their potential wells over short distances.[50] Thus, the peak frequency (f_{max}) underlies the transition from long range to short range mobility of charge carriers.[51,52]

Besides, the experimental data of M'' were fitted theoretically using a Bergman's equation which is plotted in Fig. 11(b) by a solid line. The imaginary part of $M''(\omega)$ was approximated as:[53]

$$M''(\omega) = \frac{M''_{max}}{\left((1-\beta)+\left(\frac{\beta}{1+\beta}\right)\right)\left[\beta\left(\frac{\omega_{max}}{\omega}\right)+\left(\frac{\omega}{\omega_{max}}\right)^{\beta}\right]} \quad (18)$$

with M''_{max}, ω_{max} are the modulus and the angular frequency maximum, respectively. β is the stretched exponential parameter positioned in the range of [0–1]. $\beta = 1$ for an ideal dielectric, where the dipole–dipole interaction is negligible (Debye relaxation) and this interaction is significant when $\beta < 1$ (non-Debye relaxation).

The β parameter extracted from the best fit at diverse temperatures is displayed in Fig. 12. Its values are found to be temperature dependent. We thus notice that all values of β are less than unity. This confirms the non-Debye behavior for the α-$KZnPO_4$ compound.

Activation energy associated with the relaxation process has been determined from the temperature dependent relaxation frequency, which, according to Arrhenius law, is given by:

$$f_m = f_0 \exp\left(\frac{-E_m}{k_B T}\right) \quad (19)$$

where f_0 is a pre-exponential factor, E_m is the activation energy, and k_B is the Boltzmann constant.

The insert of Fig. 13 demonstrates the plot of ln(f_m) *vs.* 1000/T. The value of activation energy (E_m) is computed according to the above plot and range in the order of (0.79 ± 0.02) eV. The

difference between the values of activation energy obtained by impedance spectroscopy and electrical relaxation modulus confirms that the transport in α-$KZnPO_4$ is not due to a simple hopping mechanism.

4. Conclusions

The α-$KZnPO_4$ compound was successfully prepared by the solid method under newly-defined conditions of temperature. X-ray diffraction recorded at room temperature revealed that the structure of the compound crystallizes in hexagonal symmetry with $P6_3$ space group. Furthermore, the EDX results confirm the good stoichiometric property of the preparation and prove a homogeneous chemical composition. The optical measurement proves the light absorption in the UV and visible range where the band gap is around 4.52 eV, indicating a wide gap semiconductor compound. A detailed analysis of the impedance data reveals a non-Debye relaxation and confirms the only contribution of grain to the conductivity of the material. An equivalent circuit for the electrochemical cell with the studied compound was proposed. The AC conductivity obeys of augmented Jonscher's power law at different temperatures. The displacements of the K^+ ion are probably due to an OLPT mechanism in the tunnel-type cavities along the *c* axis. In fact, the OLPT is the most appropriate model for explaining the mechanism of the charge transport in α-$KZnPO_4$. Values of obtained parameters from the adjustment of AC conductivity data were discussed and correlated to the crystallographic data. Eventually, the temperature variation of M'' peak showed a thermally activated relaxation process and a temperature-dependent stretching exponent β parameter.

Conflicts of interest

All authors have no conflicts of interest.

References

1 H. Sharma, S. Jindal and N. Aggarwal, Impact of copper doping on perovskite structure ferroelectric ceramic, *Mater. Today*, 2020, **33**, 1632–1636.
2 T. Xian, H. Yang, L. Di and J. Dai, Enhanced photocatalytic activity of $BaTiO3C_3N_4$ for the degradation of methyl orange under simulated sunlight irradiation, *J. Alloys Compd.*, 2015, **622**, 1098–1104.
3 P. P. Khirade, S. D. Birajdar, A. V. Humbe and K. M. Jadhav, Structural, electrical and dielectrical property investigations of Fe-doped $BaZrO_3$ nanoceramics, *J. Electron. Mater.*, 2016, **45**, 3227–3235.
4 I. Pet'kov, V. I. Korchemkin, E. A. Asabina, A. R. Zaripov, V. S. Kurazhkovskaya, E. Yu Borovikova and S. Yu Stefanovich, *Russ. J. Inorg. Chem.*, 2012, **57**, 1214–1225.
5 G. Nénert, J. Bettis, R. Kremer, H. Ben Yahia, C. S. Ritter, E. Gaudin, O. Isnard and M. H. Whangbo, *Inorg. Chem.*, 2013, **52**, 9627–9635.
6 H. P. Uppara, H. Dasari, S. K. Singh, N. K. Labhsetwar and M. S. Murari, Effect of copper doping over GdFeO3 perovskite on soot oxidation activity, *Catal. Lett.*, 2019, **149**, 3097–3110.
7 S. Zhang, D. Guo, M. Wang, M. S. Javed and C. Hu, Magnetism in $SrTiO_3$ before and after UV irradiation, *Appl. Surf. Sci.*, 2015, **335**, 115–120.
8 D. J. Shin, S. J. Jeong, C. E. Seo, K. H. Cho and J. H. Koh, Multi-layered piezoelectric energy harvesters based on PZT ceramic actuators, *Ceram. Int.*, 2015, **41**, S686–S690.
9 R. Gautier, O. K. Andersen, P. Gougeon, J. F. Halet, E. Canadell and J. D. Martin, Electronic Structure, Electrical and Magnetic Properties of RMo_8O_{14} Compounds (R = La, Ce, Pr, Nd, Sm) Containing Bicapped Mo8 Clusters, *Inorg. Chem.*, 2002, **41**, 4689–4699.
10 F. Zhou, K. Kang, T. Maxisch, G. Ceder and D. Morgan, The electronic structure and band gap of $LiFePO_4$ and $LiMnPO_4$, *Solid State Commun.*, 2004, **132**, 181–186.
11 M. D. Johannes, K. Hoang, J. L. Allen and K. Gaskell, Hole polaron formation and migration in olivine phosphate materials, *Phys. Rev. B: Condens. Matter Mater. Phys.*, 2012, **85**, 115106.
12 G. Wallez, F. Lucas, J. P. Souron and M. Quarton, Potassium-zinc monophosphate: an original polymorphic tridymite derivate, *Mater. Res. Bull.*, 1999, **34**, 1251–1261.
13 A. Martina, The Crystal Structure of α-KZnPO4, *Z. Naturforsch., B: J. Chem. Sci.*, 1992, **47**, 1249–1254.
14 R. Hammond and J. Barbier, Structural chemistry of $NaCoPO_4$, *Acta Crystallogr., Sect. B: Struct. Crystallogr. Cryst. Chem.*, 1996, **52**, 440–449.
15 P. Feng, X. Bu, S. H. Tolbert and G. D. Stucky, Syntheses and characterizations of chiral tetrahedral cobalt phosphates with zeolite ABW and related frameworks, *J. Am. Chem. Soc.*, 1997, **119**, 2497–2504.
16 R. Hammond, J. Barbier and C. Gallardo, Crystal structures and crystal chemistry of $AgXPO_4$ (X = Be, Zn), *J. Solid State Chem.*, 1998, **141**, 77–185.
17 P. Rozalin, R. Naik and N. C. Mishra, Low-temperature growth of γ phase in thermally deposited In_2Se_3 thin films, *Phase Transitions*, 2012, **91**, 862–871.
18 P. Priyadarshini, D. Subhashree, D. Alagarasan, R. Ganesan, S. Varadharajaperumal and R. Naik, Observation of high nonlinearity in Bi doped $BixIn_{35-x}Se_{65}$ thin films with annealing, *Sci. Rep.*, 2021, **11**, 21518.
19 M. Enneffati, N. K. Maaloul, B. Louati, K. Guidara and K. Khirouni, Synthesis, vibrational and UV-visible studies of sodium cadmium orthophosphate, *Opt. Quantum Electron.*, 2017, **3**, 331.
20 M. Mehnaoui, R. Ternane, G. Panczer, M. Trabelsi-Ayadi and G. Boulon, Structural and luminescent properties of new Pb^{2+} doped calcium chlorapatites $Ca_{10-x}Pb_x(PO_4)_6Cl_2$ ($0 \leq x \leq 10$, *J. Phys.: Condens. Matter*, 2008, **20**, 275227.
21 P. Priyadarshini, D. Subhashree, A. Devarajan, G. Rajamanickam and V. Selvaraj, Role of Bismuth incorporation on the structural and optical properties in BixIn35-xSe65 thin films for photonic applications, *J. Am. Ceram. Soc.*, 2021, **104**, 5803–5814.

22 P. Kubelka, Ein Beitrag zur Optik der Farbanstriche (Contribution to the optic of paint), *Z. Phys. Chem.*, 1931, **12**, 593–601.

23 K. B. Brahim, A. Oueslati, F. Hlel and M. Gargouri, Synthesis, structural characterization and electrical conduction mechanism of the new organic–inorganic complex: ($[(C_3H_7)_4N]$ $FeCl_4$), *Mater. Res. Bull.*, 2019, **118**, 110505.

24 C. L. Li, T. Y. Yan, G. O. Barasa, Y. H. Li, R. Zhang, S. Huang and S. L. Yuan, Colossal dielectric response in $Ba_{1.5}Sr_{1.5}Co_2Fe_{24}O_{41}$ ceramics at high-temperature, *J. Mater. Sci.: Mater. Electron.*, 2018, **29**, 9971–9978.

25 M. Mumtaz, M. Naveed, B. Amin, M. Imran and M. N. Khan, Temperature dependent impedance spectroscopy of (Co_3O_4) x/CuTl-1223 nanoparticles-superconductor composites, *Ceram. Int.*, 2018, **44**, 4351–4359.

26 S. B. Aziz and R. M. Abdullah, Crystalline and amorphous phase identification from the tan δ relaxation peaks and impedance plots in polymer blend electrolytes based on $[CS: AgNt]_x$: PEO (x-1)($10 \leq x \leq 50$), *Electrochim. Acta*, 2018, **285**, 30–46.

27 B. Louati, Vibrational analysis and AC electrical conduction behavior of lithium zinc orthogermanate, *Ionics*, 2021, 1–8.

28 S. Selvasekarapandian and M. Vijayakumar, The ac impedance spectroscopy studies on $LiDyO_2$, *Mater. Chem. Phys.*, 2003, **80**, 29–33.

29 I. Dakhlaoui, K. Karoui, F. Hajlaoui, N. Audebrand, T. Roisnel and F. Jomni, $[(CH_3)_3N(CH_2)_2Br]_2[CoBr_4]$ halogenometallate complex: crystal structure, high-temperature reversible phase transition, electrical and optical properties, *J. Mol. Struct.*, 2021, **1231**, 129684.

30 M. M. Costa, G. F. M. Pires Jr, A. J. Terezo, M. P. F. Graca and A. S. B. Sombra, Impedance and modulus studies of magnetic ceramic oxide $Ba_2Co_2Fe_{12}O_{22}(Co_2Y)$ doped with Bi2O3, *J. Appl. Phys.*, 2011, **110**, 034107.

31 L. Miladi, A. Oueslati and K. Guidara, Phase transition, conduction mechanism and modulus study of $KMgPO_4$ compound, *RSC Adv.*, 2016, **6**, 83280–83287.

32 L. Essaleh, S. Amhil, S. M. Wasim, G. Marín, E. Choukri and L. Hajji, Theoretical and experimental study of AC electrical conduction mechanism in the low temperature range of p-$CuIn_3Se_5$, *Phys. E Low-dimens. Syst. Nanostruct.*, 2018, **99**, 37–42.

33 J. Shanker, B. V. Prasad, M. B. Suresh, R. V. Kumar and D. S. Babu, Electrical properties of $NdCr_{1-x}Fe_xO_3$ perovskite ceramic nanoparticles—An impedance spectroscopy studies, *Mater. Res. Bull.*, 2017, **94**, 385–398.

34 S. Nasri, M. Megdiche, M. Gargouri and K. Guidara, Electrical conductivity and dielectric relaxation behavior of $AgFeP_2O_7$ compound, *Ionics*, 2014, **20**, 399–407.

35 K. Funke, Jump relaxation in solid electrolytes, *Prog. Solid State Chem.*, 1993, **22**, 111–195.

36 A. S. Nowick and B. S. Lim, Electrical relaxations: Simple versus complex ionic systems, *Phys. Rev. B: Condens. Matter Mater. Phys.*, 2001, **63**, 184115.

37 C. León, A. Rivera, A. Várez, J. Sanz, J. Santamaria and K. L. Ngai, Origin of constant loss in ionic conductors, *Phys. Rev. Lett.*, 2001, **86**, 1279.

38 I. G. Austin and N. F. Mott, Polarons in crystalline and non-crystalline materials, *Adv. Phys.*, 1969, **18**, 41–102.

39 S. R. Elliott, Ac conduction in amorphous chalcogenide and pnictide semiconductors, *Adv. Phys.*, 1987, **36**, 135–217.

40 R. Punia, R. S. Kundu, M. Dult, S. Murugavel and N. Kishore, Temperature and frequency dependent conductivity of bismuth zinc vanadate semiconducting glassy system, *J. Appl. Phys.*, 2012, **112**, 083701.

41 A. R. Long, Frequency-dependent loss in amorphous semiconductors, *Adv. Phys.*, 1982, **31**, 553–637.

42 M. Dult, R. S. Kundu, S. Murugavel, R. Punia and N. Kishore, Conduction mechanism in bismuth silicate glasses containing titanium, *Phys. Rev. B: Condens. Matter Mater. Phys.*, 2014, **452**, 102–107.

43 N. Chakchouk, B. Louati and K. Guidara, Electrical properties and conduction mechanism study by OLPT model of $NaZnPO_4$ compound, *Mater. Res. Bull.*, 2018, **99**, 52–60.

44 S. O. Mansour, B. Louati and K. Guidara, AC conductivity and dielectric behavior of low-temperature phase of α-$AgCuPO_4$, *Ionics*, 2016, **22**, 1135–1143.

45 P. B. Macedo, C. T. Moynihan and R. Bose, The long time aspects of this correlation function, which are obtainable by bridge techniques at temperatures approaching the glass transition, *Glass Phys. Chem.*, 1972, **13**, 171.

46 S. Dhankhar, R. S. Kundu, R. Parmar, S. Murugavel, R. Punia and N. Kishore, Electronic transport and relaxation studies in bismuth modified zinc boro-tellurite glasses, *Solid State Sci.*, 2015, **48**, 230–236.

47 F. S. Howell, R. A. Bose, P. B. Macedo and C. T. Moynihan, Electrical relaxation in a glass-forming molten salt, *J. Phys. Chem. A*, 1974, **78**, 639–648.

48 K. L. Nagi and C. Leon, Recent advances in relating macroscopic electrical relaxation data to microscopic movements of the ions in ionically conducting materials, *Solid State Ionics*, 1999, **125**, 81–90.

49 A. Hadded, J. Massoudi, E. Dhahri, K. Khirouni and B. F. O. Costa, Structural, optical and dielectric properties of $Cu_{1.5}Mn_{1.5}O_4$ spinel nanoparticles, *RSC Adv.*, 2020, **10**, 42542–42556.

50 K. Holderna-Natkaniec, M. O. M. Sghaier, P. Ławniczak, M. Zdanowska-Frączek, A. Wozniak-Braszak and S. Chaabouni, Electric properties and internal dynamics of the $[C_6H_{18}N_2]SbCl_5$ $[C_6H_{18}N_2]Cl_2$ in intermediate temperature phase (part II), *Polyhedron*, 2015, **85**, 131–136.

51 R. Vaish and K. B. R. Varma, Dielectric properties of Li_2O-$3B_2O_3$ glasses, *J. Appl. Phys.*, 2009, **106**, 064106.

52 N. Kaur, M. Singh, L. Singh and A. M. Awasthi, Kumar J Gamma-radiation-induced dielectric relaxation characteristics of layered crystals of phlogopite mica, *Nucl. Instrum. Methods Phys. Res., Sect. B*, 2013, **316**, 232–238.

53 R. Bergman, General susceptibility functions for relaxations in disordered systems, *J. Appl. Phys.*, 2000, **88**, 1356–1365.